Published in final edited form as:
J Xray Sci Technol. 2009 January 1; 17(4): 295–303. doi:10.3233/XST-2009-0230.

Compressive Sampling Based Interior Reconstruction for Dynamic Carbon Nanotube Micro-CT

Hengyong Yu[1], **Guohua Cao**[2], **Laurel Burk**[2], **Yueh Lee**[3], **Jianping Lu**[2], **Pete Santago**[1,4], **Otto Zhou**[2,5], and **Ge Wang**[1,4]

Hengyong Yu: hengyong-yu@ieee.org; Guohua Cao: gcao@physics.unc.edu; Laurel Burk: lmburk@physics.unc.edu; Yueh Lee: yueh_lee@med.unc.edu; Jianping Lu: jpl@physics.unc.edu; Pete Santago: psantago@wfubmc.edu; Otto Zhou: zhou@physics.unc.edu; Ge Wang: ge-wang@ieee.org

[1]Biomedical Imaging Division, VT-WFU School of Biomedical Engineering and Science, Virginia Tech, Blacksburg, VA 24061, USA

[2]Department of Physics and Astronomy, University of North Carolina, Chapel Hill, NC 27599, USA

[3]Department of Radiology, University of North Carolina, Chapel Hill, NC 27599, USA

[4]VT-WFU School of Biomedical Engineering and Science, Wake Forest University, Winston-Salem, NC 27157, USA

[5]Lineberger Comprehensive Cancer Center, University of North Carolina, Chapel Hill, NC 27599, USA

Abstract

In the computed tomography (CT) field, one recent invention is the so-called carbon nanotube (CNT) based field emission x-ray technology. On the other hand, compressive sampling (CS) based interior tomography is a new innovation. Combining the strengths of these two novel subjects, we apply the interior tomography technique to local mouse cardiac imaging using respiration and cardiac gating with a CNT based micro-CT scanner. The major features of our method are: (1) it does not need exact prior knowledge inside an ROI; and (2) two orthogonal scout projections are employed to regularize the reconstruction. Both numerical simulations and in vivo mouse studies are performed to demonstrate the feasibility of our methodology.

Keywords

Computed tomography (CT); interior tomography; compressive sampling; carbon nanotube; field emission x-ray; respiration gated

1. Introduction

Field emission x-ray source based on carbon nanotubes (CNT) is a recent invention [1-3] with several intrinsic advantages over conventional x-ray tubes with thermionic cathodes. These include high temporal resolution [1] and spatially distributed multi-beam and [2] multiplexing capabilities [3]. In addition the ease of electronic control of the radiation readily enables synchronized and/or gated imaging, which is attractive for imaging of live subjects [4,5]. Based on this new source technology, a physiologically gated micro-CT scanner with a stationary mouse bed and a rotating CNT based micro-focus x-ray source was recently developed [6]. Because of the electronic programming and fast switching capabilities of the CNT field emission x-ray source, the scanner can readily gate its imaging

acquisition to non-periodic physiological signals to provide high temporal and spatial resolutions in small animal imaging.

Interestingly, an alternative theory of compressive sampling (CS) has recently emerged that shows that high-quality signals and images can be reconstructed from far fewer data/measurements than are usually considered necessary according to the Nyquist sampling theory [7,8]. The main idea of CS is that most signals are sparse in an appropriate orthonormal system; that is, a majority of their coefficients are close or equal to zero, when represented in some domain. Typically, CS starts by taking a limited number of samples in a much less correlated basis, and the signal is exactly recovered with high probability from the limited data via the ℓ_1 norm minimization, which is also equivalent to the total variation (TV) minimization in some cases [9]. Based on the CS theory, we recently proved that if an object under reconstruction is piecewise constant, a local region-of-interest (ROI) can be exactly reconstructed via the TV minimization in the CT field [10]. Because many objects in CT applications can be approximately modeled as piecewise constant, our approach is practically useful and suggests a new research direction for interior tomography.

The combination of the CNT-based micro-CT scanner and the CS-based interior tomography technique offers many research opportunities. Here, we report our preliminary attempt to study the interior cardiac image reconstruction of a mouse with both respiratory and cardiac gating. In the next section, we report our major materials and methods. In the third section, both numerical simulation and in vivo study results are presented. In the last section, we discuss some related issues and conclude the paper.

2. Material and Method

2.1. CNT based Micro-CT Scanner

Figure 1 shows a picture of the micro-CT scanner [6], which consists of a compact CNT field emission micro-focus x-ray tube, a flat panel x-ray detector (Model C7940DK-02, Hamamatsu), a high precision rotating gantry (Model 430, HUBER, Germany), and a home-made mouse bed. The x-ray tube and the detector are mounted on two translational stages. The two translational stages are positioned on the opposite sides of the gantry, which allows independent adjustment of the source-to-object distance (SOD) and the object-to-detector distance (ODD). For this study the scanner geometry is optimized for in vivo animal studies. The SOD is 126 mm; the ODD is 39 mm. The short source-to-detector distance (SDD=165mm) and low magnification factor (M=1.3) would allow the scanner to deliver 100μm spatial resolution and 20msec temporal resolution.

The x-ray tube is a compact and portable version of the x-ray source reported in our previous work [4]. For the study reported in this paper, the x-ray tube was operated at 1mA peak tube current, 45 kV anode voltage, 112 × 152μm effective focal spot size, and 20msec pulse width. The x-ray exit window consists of 0.2mm Be. No additional filtration was used in this experiment. The x-ray detector is a CMOS flat-panel sensor with a CsI scintillator plate directly deposited on a photo diode array. It has 2400 × 2400 pixels with a nominal pixel size of 50 μm, giving an active area of 120 × 120mm^2. It has a thin carbon fiber cover and allows up to 4 × 4 on-chip binning and 9 frames/sec high-speed imaging. For this study, the camera was configured to run at 1 frame/sec and utilize only about 1/4 of its full field-of-view (FOV) at the central region without binning, producing two-dimensional 1024 × 1024 projection images at 50 μm × 50 μm pixel resolution. This detector configuration together with the scanner geometry give an effective FOV of 39 × 39mm^2 and an effective digital sampling of 38.5 μm at the object plane. The gantry is driven by a digital stepping motor (Velmex, Inc., Bloomfield, NY) and able to travel a full circle with a resolution of 0.001 degree.

The scanner is controlled by a home-made computer program written in LabVIEW (National Instruments, Austin, TX). At the beginning of each CT scan, the LabVIEW program performs a series of initialization steps, which includes homing the gantry to its zero position. The program then instructs the x-ray tube, the detector, the gantry, and a home-made dynamic gating electronic circuits (if gating is involved), to work sequentially so that projection images are acquired in the step-and-shoot mode. Multiple-frame acquisition is also allowed for frame averaging. At the end of scan, the LabVIEW program rewinds the goniometer to its zero position.

2.2. CS based Interior Tomography Algorithm

Based on the CS theory, we have recently found that a local ROI can be exactly and stably reconstructed via the total variation minimization if the object under reconstruction is piecewise constant [10]. Let (ρ,θ) be a 2D polar coordinate system, the ℓ_1 norm of the image $f(\rho,\theta)$ inside the ROI can be mathematically expressed as:

$$f_{tv}=\int_0^{2\pi} d\theta \int_0^{\rho_0} |\mu(\rho,\theta)|\rho d\rho, \tag{1}$$

where $\mu(\rho,\theta)$ represents a sparsifying transform of $f(\rho,\theta)$. For the commonly used gradient transform in the medical imaging field, we have

$$\mu(\rho,\theta)=\sqrt{\left(\frac{\partial f(\rho,\theta)}{\partial\rho}\right)^2+\left(\frac{\partial f(\rho,\theta)}{\rho\partial\theta}\right)^2}, \tag{2}$$

which is the gradient magnitude or absolute value of the maximum directional derivation at (ρ,θ). Typically, $\mu(\rho,\theta)$ defined by Eqs. (1) and (2) represents the total variation. When there exists an artifact image $g(\rho,\theta)$ due to a data truncation outside a central ROI of radius ρ_0, the total variation becomes

$$\tilde{f}_{tv}=\int_0^{2\pi} d\theta \int_0^{\rho_0} \rho d\rho \sqrt{\left(\frac{\partial f(\rho,\theta)}{\partial\rho}+\lambda\frac{\partial g(\rho,\theta)}{\partial\rho}\right)^2+\left(\frac{\partial f(\rho,\theta)}{\rho\partial\theta}+\lambda\frac{\partial g(\rho,\theta)}{\rho\partial\theta}\right)^2}, \tag{3}$$

where λ is a coefficient. Recently, we contributed to the CS theory by proving the following theorem for exact interior tomography [10].

Theorem 1: *In the compressive sampling framework, an interior ROI of a general compactly supported function* ***f*** *can be exactly determined by minimizing the total variation defined by* Eq. (3) *if* ***f*** *can be decomposed into finitely many constant subregions*.

The major idea of our proof is that $\tilde{f}_{tv}$ can be minimized at $\lambda = 0$ for the given $f(\rho,\theta)$ and $g(\rho,\theta)$. Because many objects in CT applications can be approximately modeled as piecewise constant, Theorem 1 is practically useful and suggests a new research direction of interior tomography. For practical applications, it is the common case to acquire two global orthogonal scout projections to locate an ROI. Hence, it is a natural choice for us to employ two scout images to regularize our CS-based local reconstruction. Note that the use of scout images has not been reported elsewhere, and this may be considered a contribution of our work.

To perform interior reconstruction from data collected on the CNT based micro-CT scanner mentioned in 2.1, we developed a numerical algorithm in the CS framework. This algorithm is a modification of our previous version [10] and it consists of two major steps. In the first step, the ordered-subset simultaneous algebraic reconstruction technique (OS-SART) [11] was used to reconstruct a digital image $f_{m,n} = f(m\Delta, n\Delta)$ based on all the available local and scout projections, where Δ represents the sampling interval, m and n are integers. In the second step, we minimize the ℓ_1 norm for the discrete gradient transform of $f_{m,n}$ using the standard steepest descent method. These two steps were iteratively performed in an alternating manner. Specifically, the algorithm can be summarized in the following pseudo-code [8,10,12,13]:

S1. Initialize control parameters α, α_s, P_{TV}, and P_{ART};

S2. Initialize reconstruction $k := 0$ and $f^0_{m,n}=0$;

S3. Perform OS-SART reconstruction and TV minimization alternately

S3.1 Initialize the loop $k := k + 1$; $f^k_{m,n}:=f^{k-1}_{m,n}$;

S3.2 Perform reconstruction for every projection subset p_{art} to P_{ART}

S3.2.1 Perform OS-SART reconstruction

S3.2.1.1 Forward compute the current projections of $f^k_{m,n}$ in the p_{art} subset;

S.3.2.1.2 Update $f^k_{m,n}$ by backprojecting the projection errors in the p_{art} subset;

S.3.2.2 Minimize TV by steepest descent method for $p_{tv} = 1$ to P_{TV} to

S.3.2.2.1 Compute the steepest decent direction $d_{m,n}$;

S.3.2.2.2 Compute normalized coefficient

$$\beta:=\max(|f^k_{m,n}|)\div\max(|d_{m,n}|);$$

S.3.2.2.3 Update the reconstructed image

$$f^k_{m,n}=f^k_{m,n}-\alpha\times\beta\times d_{m,n};$$

S.3.2.2.4 Update the control parameter $\alpha = \alpha \times \alpha_s$;

S3.3 Check the stopping criteria

S1 initializes the control parameters α, α_s, P_{TV} and P_{ART}, where α represents the maximal step for the steepest descent to minimize TV, α_s the decreasing scale of α after each computation, P_{TV} the local loop time to minimize TV, and P_{ART} denotes the number of subsets for OS-SART reconstruction. S2 initializes the reconstructed image and the main loop count k for alternating iteration procedure S3. S3.2.1.1 computes the forward projections of the current image in the p_{art} subset, where it may include both local truncated and global scout projections. In our code, we employ a global imaging geometry and adapt a projection mask image to indicate which pixel in the projection domain is available. S3.2.1.2 updates $f^k_{m,n}$ by backprojecting the projection differences, where only the projections in p_{art} subset are used. S3.2.2 define the local loop to minimize the ℓ_1 norm. S3.3 decides if the main loop should be stopped or not.

Our algorithm was numerically implemented in MatLab on a PC (4.0 Gigabyte memory, 3.16G Hz CPU). While the basic structure was constructed in MatLab, all the

computationally intensive parts were coded in C, which was linked via a MEX interface. A maximal iteration time was set to stop the main loop. Different from our previous exact knowledge based interior tomography algorithms [14-19] in terms of both projection onto convex sets (POCS) [15] and singular value decomposition (SVD) [18,19], the CS based interior reconstruction proposed in this paper only uses some imaging model instead of exact knowledge, and it employs two scout images to improve image quality.

3. Results and Analysis

3.1. Numerical Simulation

In our numerical simulation, we assumed a circular scanning locus of radius 57.0 cm and a fan-beam imaging geometry. We also assumed an equi-spatial virtual detector array of length 20.0 cm. The detector was centered at the system origin and made always perpendicular to the direction from the system origin to the x-ray source. The detector array included 600 elements, each of which is of aperture 0.033 cm. For a complete scanning turn, we equi-angularly collected 650 projections. In our simulation, we first acquired two complete nontruncated projections (50^{th} and 213^{th} acquisition angles) to serve as scout images, then performed an ROI full scan to acquire truncated projections, each of which covered central 240 elements. Therefore, this scanning configuration covered a circular ROI of radius 3.990 cm. The imaging subject was a 2D modified Shepp-Logan phantom within a FOV of radius 10 cm [10]. The reconstructed images were in a 256×256 matrix covering the whole FOV and the reconstruction times were 59 minutes for 100 iterations. The control parameters were $\alpha = 0.005$, $\alpha_s = 0.995$, $P_{TV} = 2$, and $P_{ART} = 26$. As a comparison, we also reconstructed an image by a local FBP method combining smooth extrapolation for the truncated projection data. While the typical reconstructed images were shown in Figure 2, the typical profiles were plotted in Figure 3. As seen from Figures 2 and 3, the reconstructed images from the proposed algorithm have a very high precision inside the ROI. However, there are still some differences between the phantom images and the reconstructed images (see Fig. 3 (b)). As we explained in our previous work [10], the reasons are as the follows. First, the discrete projections and images are sampling of the original ones in continuous domain on the sampling grids. From the viewpoint of signal processing, the sampling process will serve as a truncation function in frequency domain. The reconstructed images will not satisfy the piecewise constant condition due to the high-frequency truncation. Second, the reconstruction results convergence to the real values only when the iteration times trend to infinite. Hence, the finite iteration time will compromise the reconstruction results.

3.2. Animal Studies

In vivo mouse imaging experiments were performed following the protocols approved by the University of North Carolina at Chapel Hill. Several mice with an average weight of 25 grams were imaged. Animals were anesthetized with 1–2% isoflurane at a flow rate of 1.5–2L/min from a vaporizer. The animal breathing rates after anesthetization were typically in the range of 80–100breaths/min. A physiological monitoring system (BioVet, Spin Systems (QLD) Pty Ltd, Brisbane, Australia) was used to obtain the cardiac and respiration signals. The anesthetized animals were placed on top of the pressure sensor in the mouse sample holder and secured with adhesive restraints. The animals were put in the prone position such that the respiration sensor was approximately in the position of the abdomen to achieve maximum sensor coupling. To obtain the cardiac signals, ECG electrodes were taped to the footpads. Prior to imaging, iodinated contrast agent (Fenestra VC, Advanced Research Technologies Inc., Montreal, Canada) was infused via tail vein injection (0.02mL/gram of mouse).

Projection images were acquired using a prospective gating approach, where the gating electronics is same as the one described in our previous work [4], except that in this study the physiological triggers were generated based on both respiration and cardiac gating. Physiological triggers were generated if and only if the first QRS complex of the ECG occurred within an acquisition window defined at a specific phase of the respiration cycle. For CT scans carried out in this study, 400 projections were acquired over a circular orbit of 199.5 degrees with a stepping angle of 0.5 degree at single frame acquisition. By running the detector at 1 frame/sec (camera integration time = 500ms), the scan time was 15-30min, depending the mouse's respiration and heart rates. This scan time is critically depending on the temporal coincidence between the physiological triggers and the exposure windows, in addition to the temporal coincidence between the QRS complex of ECG and the acquisition window of the respiration signal.

For the above acquired in vivo mouse cardiac projection datasets, we performed a CS-based interior reconstruction. Using the generalized Feldkamp algorithm [20,21], first we reconstructed a volumetric image to serve as a global standard for our interior reconstruction. From such an image volume, we specified a circular ROI on a transverse slice to cover the contrast-enhanced beating heart. Then, we created a mask image for the ROI and performed a forward projection to generate a mask projection. Later the mask projection was binarized to extract the projection data only through the ROI as our interior scan dataset. Meanwhile, the global projections of 1^{st} and 360^{th} were kept to serve as two scout images. The interior reconstruction was performed using our CS based algorithm described in section II; the control parameters were $\alpha = 0.005$, $\alpha_s = 0.997$, $P_{TV} = 2$, and $P_{ART} = 20$. The final reconstruction results are in Figure 4. Because the CS-based iterative reconstruction framework is capable of noise removing, our CS-based interior reconstruction result has a high SNR than that of the global FBP reconstruction.

While the radiation dose to the whole body can be reduced using our reconstruction method by limiting the x-ray beam to the ROI only, the organ dose—the dose of the organ which happens to be within the ROI under interior reconstruction—would remain at the same level. Because the CS reconstruction theory is based on the so-called sparsifying transform, the radiation dose of local ROI can be further reduced with fewer projection views. However, the smaller the number of projections, the worse the reconstructed image quality [13]. To study how the projection number affects the reconstructed image quality, 200/100/50 projections were uniformly selected from the above mentioned projections by discarding 1/3/7 projections in every 2/4/8/ projections. For these reduced projections, we can save radiation dose 50%, 75% and 87.5%, respectively. During the reconstruction procedure, two global orthogonal scout projections were also employed. The reconstructed results were shown in Figure 5. It can be seen that the image quality was good enough even using only 100 projections.

4. Discussions and Conclusion

The major advantage of our interior tomography algorithm lies in the fact that it only needs the local projection data passing through the ROI. Hence, it can help to reduce radiation dose, speedup detector readout rate, improve temporal resolution, etc. However, the current configuration of our micro-CT system covers the whole mouse body. While the global datasets can help demonstrate the feasibility of our interior tomography algorithm for physiologically gated mouse cardiac imaging, it does have redundant data. In the future, we will design a specific collimator to restrict the x-ray beam to a targeted ROI, such as the mouse heart. It is also possible for us to develop a new type source whose beam width is adjustable. We will report our results along this direction in follow up papers.

In conclusion, we have applied the CS based interior tomography algorithm for mouse cardiac imaging using respiratory and cardiac gated technique on a CNT based micro-CT scanner. Combining CS based interior tomography and CNT based micro-CT system is a novel idea, and there are many new opportunities for us to improve the cardiac imaging temporal resolution for animal studies. The introduction of two global scout images for reconstruction is another contribution of this work.

Acknowledgments

This work done at Virginia Tech is partially supported by NIH/NIBIB grants (EB002667, EB004287, EB007288). And this work done at UNC is supported by grants from NIBIB (4R33EB004204), NCI (U54CA119343), UNC University Cancer Research Fund, and Xintek.

References

1. Cheng Y, et al. Dynamic radiography using a carbon-nanotube-based field-emission x-ray source. Review of Scientific Instruments 2004;75(10):3264–3267.
2. Zhang J, et al. Stationary scanning x-ray source based on carbon nanotube field emitters. Applied Physics Letters 2005;86(18)
3. Liu ZJ, et al. Carbon nanotube based microfocus field emission x-ray source for microcomputed tomography. Applied Physics Letters 2006;89(10)
4. Cao, G., et al. Medical Imaging 2008 Conference. San Diego, CA: Spie-Int Soc Optical Engineering; 2008. Respiratory-gated micro-CT using a carbon nanotube based micro-focus field emission x-ray source - art. no. 691304.
5. Cao G, et al. A dynamic micro-CT scanner based on a carbon nanotube field emission x-ray source. Physics in Medicine and Biology 2009;54:2323–2340. [PubMed: 19321922]
6. Cao G, et al. A dynamic micro-CT scanner with a stationary mouse bed using a compact carbon nanotube field emission x-ray tube. SPIE-Medical Imaging 2009. 2009
7. Donoho DL. Compressed sensing. IEEE Transactions on Information Theory 2006;52(4):1289–1306.
8. Candes EJ, Romberg J, Tao T. Robust uncertainty principles: Exact signal reconstruction from highly incomplete frequency information. IEEETransactions on Information Theory 2006;52(2): 489–509.
9. Rudin LI, Osher S, Fatemi E. Nonlinear Total Variation Based Noise Removal Algorithms. Physica D 1992;60(1-4):259–268.
10. Yu HY, Wang G. Compressed sensing based Interior tomography. Phys Med Biol 2009;54(9): 2791–2805. [PubMed: 19369711]
11. Wang G, Jiang M. Ordered-Subset Simultaneous Algebraic Reconstruction Techniques (OS-SART). Journal of X-ray Science and Technology 2004;12(3):169–177.
12. Candes E, Romberg J. Signal Recovery from Random Projections. Computational Imaging III, Proceedings of SPIE 2005;5674
13. Chen GH, Tang J, Leng S. Prior image constrained compressed sensing (PICCS): A method to accurately reconstruct dynamic CT images from highly undersampled projection data sets. Medical Physics 2008;35(2):660–663. [PubMed: 18383687]
14. Wang, G.; Ye, YB.; Yu, HY. General VOI/ROI Reconstruction Methods and Systems using a Truncated Hilbert Transform. Patent disclosure submitted to Virginia Tech. Intellectual Properties on May 15, 2007. 2007.
15. Ye YB, et al. A general local reconstruction approach based on a truncated Hilbert transform. International Journal of Biomedical Imaging, 2007. 2007 Article ID: 63634, 8 pages.
16. Ye YB, Yu HY, Wang G. Exact interior reconstruction from truncated limited-angle projection data. International Journal of Biomedical Imaging, 2008. 2008 Article ID: 427989, 6 pages.
17. Ye YB, Yu HY, Wang G. Exact Interior Reconstruction with Cone-beam CT. International Journal of Biomedical Imaging, 2007. 2007 Article ID: 10693, 5 pages.

18. Yu HY, Ye YB, Wang G. Local Reconstruction Using the Truncated Hilbert Transform via Singular Value Decomposition. Journal of X-Ray Science and Technology 2008;16(4):243–251.
19. Wang G, Yu HY, Ye YB. A scheme for multi-source interior tomography. Med Phys 2009;36:3575–3581. [PubMed: 19746792]
20. Feldkamp LA, Davis LC, Kress JW. Practical cone-beam algorithm. J Opt Soc Am 1984;1(A): 612–619.
21. Wang G, et al. A General Cone-Beam Reconstruction Algorithm. IEEE Transactions on Medical Imaging 1993;12(3):486–496. [PubMed: 18218441]

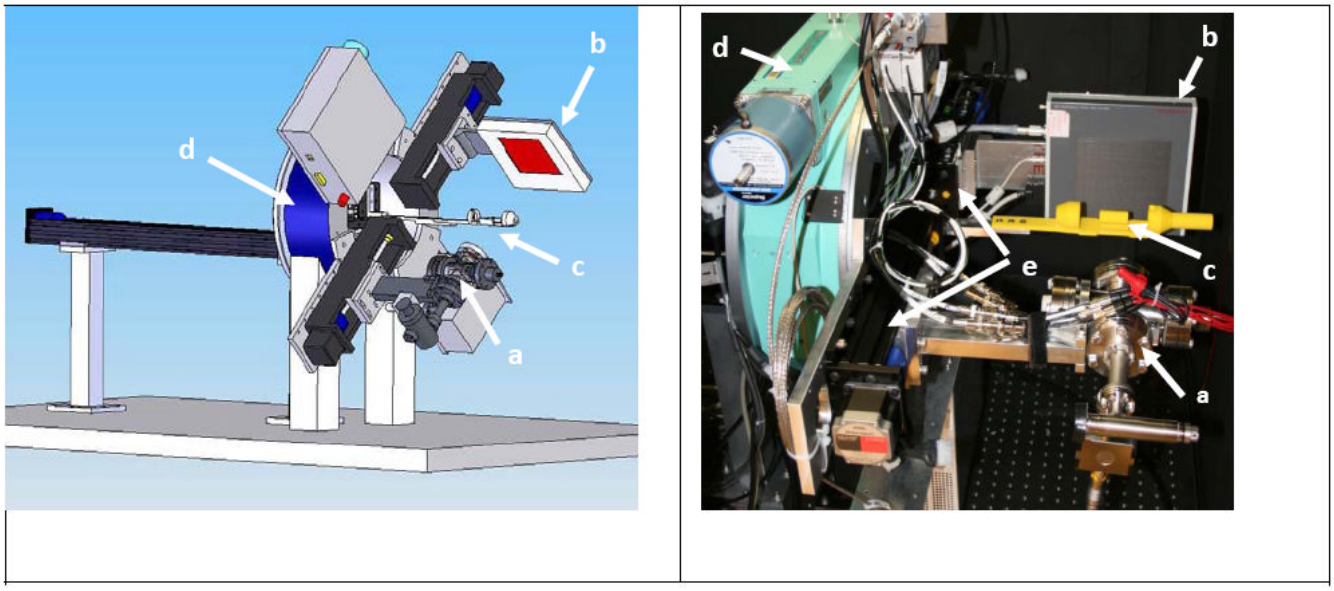

Figure 1.

Dynamic micro-CT system using the CNT x-ray tube technology. Left: A CAD rendering of the dynamic micro-CT scanner architecture. Right: A photograph of the opened scanner. The key components include (a) a CNT micro-focus x-ray tube and (b) a CCD detector that can be rotated around (c) a mouse positioning stage to collect projection data, as well as (d) a goniometer to mount the tube and detector and (e) translational stages to adjust the position of the imaging chain relative to the mouse holder.

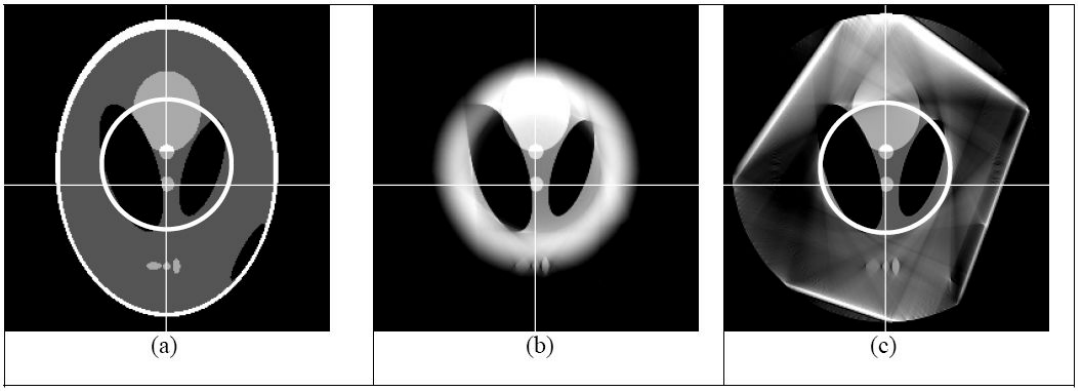

Figure 2.
Reconstruction of the modified Shepp-Logan phantom [11]. (a) The original phantom, (b) the reconstruction using the local FBP (after smooth data extrapolation) and (c) the reconstruction using the proposed CS-based interior tomography algorithm after 100 iterations. The display window is [0.1,0.4].

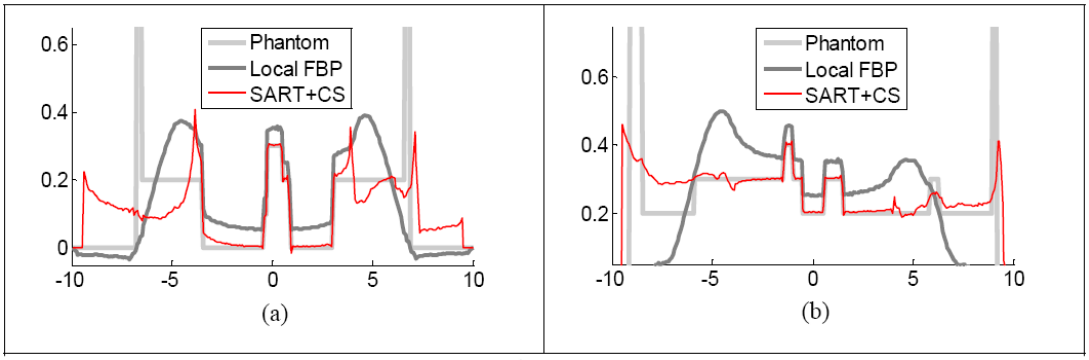

Figure 3.
Representative profiles along the white lines in Figure 2.

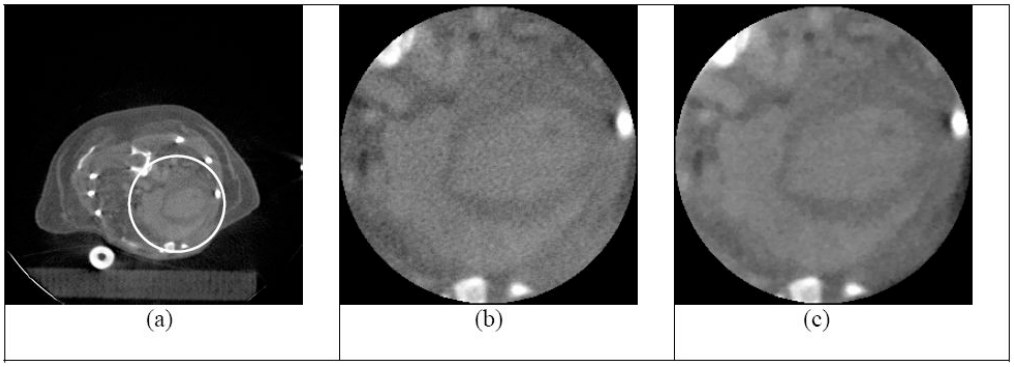

Figure 4.
Compressive-sampling-based interior tomography of a mouse chest using the CNT-based x-ray source gating technique. (a) The image reconstructed from a complete global dataset as the gold standard with the white circle for a cardiac ROI, (b) the local magnification of the ROI in (a) and (c) the interior tomography reconstruction from 400 projections after 60 iterations (without precise knowledge of a subregion in the ROI).

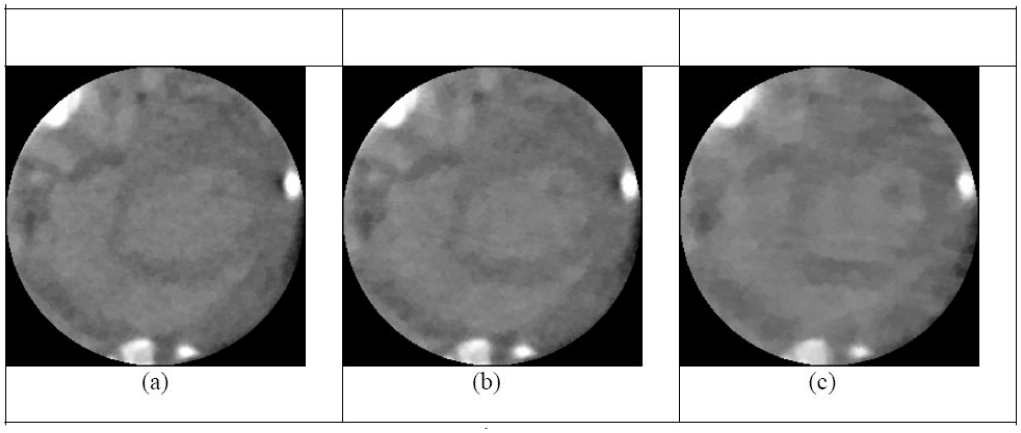

Figure 5.
Compressive-sampling-based interior tomography of a mouse chest using (a) 200, (b) 100 and (c) 50 projections to reduce the radiation dose to 50%, 25% and 12.5% of that for Figure 4(c), respectively.